

# Electronic structure and excited-state properties of $\text{Co}_2\text{TiSn}$ and $\text{Co}_2\text{ZrSn}$ from ab initio calculations

L.V.Bekenov<sup>1</sup>, V.N.Antonov<sup>1</sup>, A.P.Shpak<sup>1</sup>, A.N.Yaresko<sup>2</sup>

<sup>1</sup> Institute of Metal Physics,  
36 Vernadsky Street, 252142 Kiev, Ukraine

<sup>2</sup> Max Planck Institute for Physics of Complex Systems,  
D–01187 Dresden, Germany

Received June 24, 2005

The electronic structure, magnetism as well as the excited-state properties such as the optical and x-ray magnetic circular dichroism (XMCD) spectra of the Heusler alloys  $\text{Co}_2\text{TiSn}$  and  $\text{Co}_2\text{ZrSn}$  were investigated theoretically from first principles using the fully relativistic Dirac LMTO band structure method. The origin of the XMCD spectra at the Co  $L_{2,3}$  edges in the compounds is examined. Densities of valence states, orbital and spin magnetic moments as well as optical spectra are analyzed and discussed. The calculated results are compared with the available experimental data.

**Key words:** *electronic structure, Heusler alloys, x-ray magnetic circular dichroism, optics*

**PACS:** *71.28.+d, 71.25.Pi, 75.30.Mb*

## 1. Introduction

Heusler intermetallic alloys have attracted great interest during the last century due to the possibility to study, in the same family of alloys, a series of interesting diverse magnetic phenomena like itinerant and localized magnetism, antiferromagnetism, helimagnetism, Pauli paramagnetism, or heavy-fermionic behaviour [1–3]. Recently the rapid development of spintronics [4–7] intensified the interest in the Heusler alloys [8]. Most magnetoelectronic devices rely on an imbalance in the number of majority and minority spin carriers, with the ideal material exhibiting a complete (100%) spin-polarization at the Fermi surface (i.e., a half-metallic ferromagnet) [9], and some of the Heusler compounds have been predicted from first-principles calculations to be half-metallic [9–11].

Theoretical and experimental investigations of the  $\text{Co}_2\text{TiSn}$  and  $\text{Co}_2\text{ZrSn}$  Heusler alloys have been performed for a few decades [12–19].  $\text{Co}_2\text{TiSn}$  and  $\text{Co}_2\text{ZrSn}$  have

been found to be ferromagnets with Curie temperatures ( $T_C$ ) around 371 and 448 K, respectively [12,15]. The saturation magnetic moments estimated from magnetization measurements at 4.2 K in a field of 18 kOe for  $\text{Co}_2\text{TiSn}$  and  $\text{Co}_2\text{ZrSn}$  are reported to be  $1.96 \mu_B$  and  $1.46 \mu_B$  per formula unit (f.u.), respectively [15]. Very similar results were obtained by the authors of [18], whose high-field magnetization measurements up to 150 kOe at 4.2 K gave  $1.92 \mu_B/\text{f.u.}$  for  $\text{Co}_2\text{TiSn}$  and  $1.64 \mu_B/\text{f.u.}$  for  $\text{Co}_2\text{ZrSn}$ . The ferromagnetic behaviour of the considered alloys results from the presence of a large amount of the magnetic Co atoms. It is interesting to note that the corresponding Ni compounds are Pauli paramagnets, and by varying the Ni/Co ratio, it is possible to change their paramagnetic behaviour to ferromagnetic one; for  $\text{Ni}_{2-x}\text{Co}_x\text{TiSn}$  such a change occurs at  $x = 1.2$  [16].

The electronic structure calculations of the  $\text{Co}_2\text{TiSn}$  alloy using the symmetrized augmented plane-wave (SAPW) method were carried out in [14]. It was found that the Co  $d$  bands are characterized by the hump near the Fermi level of the DOS curves and are mainly occupied for both spin states, while the major peaks of the Ti  $d$  states lie in the high energy region and are mainly unoccupied in both spin states. The reported evaluated total magnetic moment values strongly depend on the exchange parameters which were used to form the crystal potential from a superposition of the atomic potentials. The authors of [17] presented the outcome of high-resolution x-ray photoemission spectroscopy measurements of the  $\text{Co}_2\text{ZrSn}$  valence bands in comparison with the total density of states distribution curves obtained from their band structure calculations of  $\text{Co}_2\text{ZrSn}$ , which were fulfilled by means of the spin-polarized tight-binding linear muffin-tin orbital (TBLMTO) method, and found a very good agreement between the experimental and theoretical results. The total magnetic moment was obtained to be  $1.74 \mu_B/\text{f.u.}$ .

The x-ray magnetic circular dichroism technique developed in recent years has evolved into a powerful magnetometry tool to separate orbital and spin contributions to element specific magnetic moments. X-ray magnetic circular dichroism experiments measure the absorption of x-rays with opposite (left and right) states of circular polarization. Recently x-ray magnetic circular dichroism in  $\text{Co}_2\text{TiSn}$  and  $\text{Co}_2\text{ZrSn}$  has been measured at the Co  $L_{2,3}$  edges [18]. Using the magneto-optic sum rules the spin moment and the orbital moment of Co for  $\text{Co}_2\text{TiSn}$  have been deduced to be  $0.87$  and  $0.09 \mu_B$ , respectively, and for  $\text{Co}_2\text{ZrSn}$   $0.7$  and  $0.12 \mu_B$ . The authors also calculated the Co  $3d$  partial density of states using the LMTO-ASA band structure method to interpret the XMCD spectra. However, they did not include the spin-orbit (SO) interaction in their calculations and, hence, were not able to obtain the orbital moment.

Optical properties investigations of  $\text{Co}_2\text{TiSn}$  and  $\text{Co}_2\text{ZrSn}$  exhibit abnormal behaviour of the real part of the dielectric function  $\epsilon_1(\omega)$ , which becomes negative only at the wave lengths greater than  $4 \mu\text{m}$  for  $\text{Co}_2\text{TiSn}$  and  $13 \mu\text{m}$  for  $\text{Co}_2\text{ZrSn}$  and which module values  $|\epsilon_1|$  are comparatively low, and the real part of the optical conductivity  $\sigma_1(\omega)$ , which does not show the Drude-like behaviour at low energies [19].

The aim of this work is the theoretical investigation of the electronic structure of  $\text{Co}_2\text{TiSn}$  and  $\text{Co}_2\text{ZrSn}$  Heusler alloys using the fully relativistic Dirac LMTO band

structure method. We calculated the x-ray absorption as well as the x-ray magnetic circular dichroism spectra in these compounds and the energy dependences of some of the optical characteristics.

This paper is organized as follows. Section 2 presents a description of the  $\text{Co}_2\text{TiSn}$  and  $\text{Co}_2\text{ZrSn}$  Heusler alloys crystal structure and the computational details. Section 3 is devoted to the electronic structure, XMCD spectra, magnetic and optical properties of the alloys calculated in the fully relativistic Dirac LMTO band structure method. Finally, the results are summarized in section 4.

## 2. Crystal structure and computational details

The Heusler-type  $\text{Co}_2\text{TiSn}$  and  $\text{Co}_2\text{ZrSn}$  have a cubic  $L2_1$  structure (space group  $Fm\bar{3}m$ ), which can be thought of as a simple cubic lattice for Co atoms, with the Sn and Ti or Zr atoms arranged at alternate body centered positions. The Co, Ti and Zr atoms have eight nearest neighbors at the same distance. Ti and Zr has eight Co atoms as nearest neighbors, while for Co there are four Ti or Zr and four Sn atoms.

The electronic structures of the alloys were calculated for the experimentally observed lattice constants [13], which are  $a = 11.4517$  a.u. for  $\text{Co}_2\text{TiSn}$  and  $a = 11.8051$  a.u. for  $\text{Co}_2\text{ZrSn}$ , using the spin-polarized fully relativistic linear-muffin-tin-orbital (SPR LMTO) method [20,21] in the atomic sphere approximation (ASA) with the combined correction term taken into account. The LSDA part of the calculations was based on the spin-density functional with the von Barth-Hedin parametrization [22] of the exchange-correlation potential. Brillouin zone (BZ) integrations were performed using the improved tetrahedron method [23] and charge self-consistency was obtained on a grid of 641  $\mathbf{k}$  points in the irreducible wedge of the BZ. The basis consisted of  $s$ ,  $p$  and  $d$  LMTO's.

Once energies  $\epsilon_{\mathbf{k}n}$  and functions  $|\mathbf{k}n\rangle$  for the  $n$  bands are obtained self-consistently, the interband contribution to the imaginary part of the dielectric tensor  $\epsilon_2(\omega)$  can be calculated by summing transitions from occupied to unoccupied states (with fixed  $\mathbf{k}$  vector) over the BZ, weighted with the appropriate matrix element for the probability of the transition. To be specific, the components of  $\epsilon_2(\omega)$  are given by

$$\begin{aligned} \epsilon_2^{ij}(\omega) &= \frac{Ve^2}{2\pi\hbar m^2\omega^2} \int d^3k \sum_{nn'} \langle \mathbf{k}n | p_i | \mathbf{k}n' \rangle \langle \mathbf{k}n' | p_j | \mathbf{k}n \rangle \\ &\times f_{\mathbf{k}n} (1 - f_{\mathbf{k}n'}) \delta(\epsilon_{\mathbf{k}n'} - \epsilon_{\mathbf{k}n} - \hbar\omega). \end{aligned} \quad (1)$$

Here  $(p_x, p_y, p_z) = \mathbf{p}$  is the momentum operator and  $f_{\mathbf{k}n}$  is the Fermi distribution. Further details about the evaluation of matrix elements are given elsewhere [24,25]. The real part of the components of the dielectric tensor  $\epsilon_1(\omega)$  is then calculated using the Kramer-Kronig transformation. Knowledge of both the real and imaginary parts of the dielectric tensor permits the calculation of important optical constants. The calculations yield unbroadened functions. To reproduce the experimental conditions more correctly, it is necessary to broaden the calculated spectra, although the exact form of the broadening function is unknown. Also the instrumental resolution

smears out many fine features. To simulate these effects the lifetime broadening was simulated by convoluting the calculated optical constants with a Lorentzian, and the experimental resolution was simulated by broadening the final spectra with a Gaussian.

In order to calculate the XMCD properties one has to take into account both magnetism and SO coupling when dealing with the electronic structure of the material considered, since the symmetry reduction in comparison with the paramagnetic state, which causes XMCD effect and is due to magnetic ordering, has consequences only when SO coupling is considered in addition [26].

Within the one-particle approximation, the absorption coefficient  $\mu$  for incident x-rays of polarization  $\lambda$  and photon energy  $\hbar\omega$  can be determined as the probability of electron transitions from an initial core state (with wave function  $\psi_j$  and energy  $E_j$ ) to the final unoccupied states (with wave functions  $\psi_{n\mathbf{k}}$  and energies  $E_{n\mathbf{k}}$ )

$$\mu_j^\lambda(\omega) = \sum_{n\mathbf{k}} |\langle \Psi_{n\mathbf{k}} | \mathcal{J}_\lambda | \Psi_j \rangle|^2 \delta(E_{n\mathbf{k}} - E_j - \hbar\omega) \theta(E_{n\mathbf{k}} - E_F), \quad (2)$$

with  $\mathcal{J}_\lambda = -e\boldsymbol{\alpha}\mathbf{a}_\lambda$  being the dipole electron-photon interaction operator, where  $\boldsymbol{\alpha}$  are Dirac matrices,  $\mathbf{a}_\lambda$  is the  $\lambda$  polarization unit vector of the photon vector potential [ $a_\pm = 1/\sqrt{2}(1, \pm i, 0)$ ,  $a_z = (0, 0, 1)$ ]. (Here  $+/-$  denotes, respectively, left and right circular photon polarizations with respect to the magnetization direction in the solid).

In order to simplify the comparison of the theoretical x-ray isotropic absorption  $L_{2,3}$  spectra of  $\text{Co}_2\text{TiSn}$  and  $\text{Co}_2\text{ZrSn}$  with the experimental ones we take into account the background intensity which affects the high energy part of the spectra. The shape of x-ray absorption caused by the transitions from inner levels to the continuum of unoccupied levels was first discussed by Richtmyer *et al.* in the early thirties [27]. The absorption coefficient with the assumption of equally distributed empty continuum levels is

$$\mu(\omega) = \frac{C\Gamma_c}{2\pi} \int_{E_{cf_0}}^{\infty} \frac{dE_{cf}}{(\Gamma_c/2)^2 + (\hbar\omega - E_{cf})^2}, \quad (3)$$

where  $E_{cf} = E_c - E_f$ ,  $E_c$  and  $\Gamma_c$  are the energy and the lifetimes broadening of the core hole,  $E_f$  is the energy of empty continuum level,  $E_{f_0}$  is the energy of the lowest unoccupied continuum level, and  $C$  is a normalization constant which in this paper has been used as an adjustable parameter.

Finally, the intrinsic broadening mechanisms have been considered by folding XMCD spectra with a Lorentzian. For the finite lifetime of the core hole a constant width  $\Gamma_c$ , in general from [28], has been used. The finite apparatus resolution of the spectrometer has been considered by means of a Gaussian.

Concurrent with the x-ray magnetic circular dichroism experimental developments, some important magneto-optical sum rules have been derived in recent years [29].

For the  $L_{2,3}$  edges the  $l_z$  sum rule can be written as

$$\langle l_z \rangle = n_h \frac{4 \int_{L_3+L_2} d\omega (\mu_+ - \mu_-)}{3 \int_{L_3+L_2} d\omega (\mu_+ + \mu_-)}, \quad (4)$$

where  $n_h$  is the number of holes in the  $d$  band  $n_h = 10 - n_d$ ,  $\langle l_z \rangle$  is the average of the magnetic quantum number of the orbital angular momentum. The integration is taken over the whole  $2p$  absorption region. The  $s_z$  sum rule is written as

$$\langle s_z \rangle + \frac{7}{2} \langle t_z \rangle = n_h \frac{\int_{L_3} d\omega (\mu_+ - \mu_-) - 2 \int_{L_2} d\omega (\mu_+ - \mu_-)}{\int_{L_3+L_2} d\omega (\mu_+ + \mu_-)}, \quad (5)$$

where  $t_z$  is the  $z$  component of the magnetic dipole operator  $\mathbf{t} = \mathbf{s} - 3\mathbf{r}(\mathbf{r} \cdot \mathbf{s})/|\mathbf{r}|^2$  which takes into account the asphericity of the spin moment. The integration  $\int_{L_3}$  ( $\int_{L_2}$ ) is taken only over the  $2p_{3/2}$  ( $2p_{1/2}$ ) absorption region.

### 3. Results and discussion

#### 3.1. Electronic structure

The fully relativistic spin-projected energy band structures and total DOS of  $\text{Co}_2\text{TiSn}$  and  $\text{Co}_2\text{ZrSn}$  obtained from our LSDA calculations are presented in figure 1. As one can see, the band structures of both alloys are quite similar, though it is evident that there are some differences in the DOS of these Heusler compounds due to both the presence of different atoms and different volumes. The occupied part of

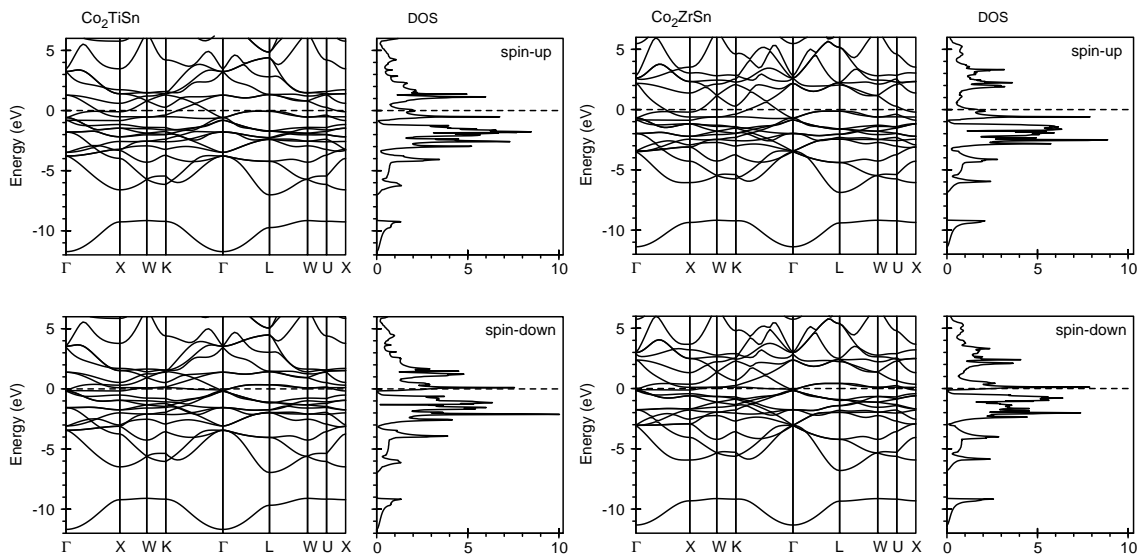


**Figure 1.** Self-consistent fully relativistic spin-polarized LSDA energy band structures and total DOS (in states/(cell eV)) of  $\text{Co}_2\text{TiSn}$  and  $\text{Co}_2\text{ZrSn}$ .

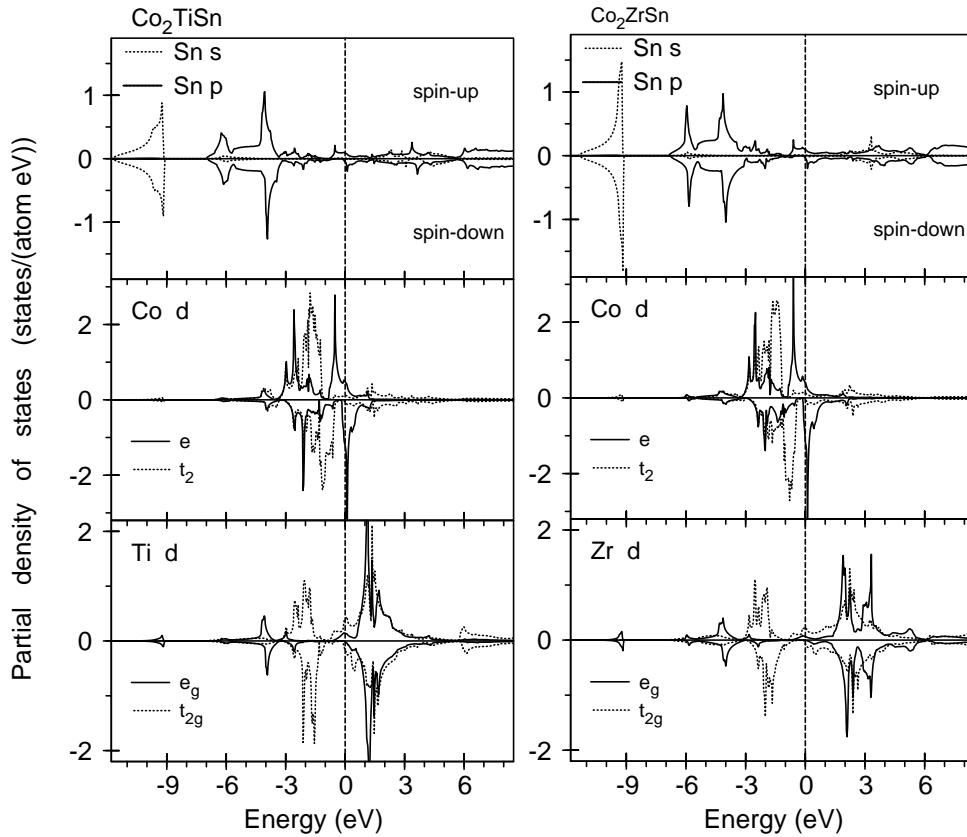


**Figure 2.** Symmetry separated partial density of states of  $\text{Co}_2\text{TiSn}$  and  $\text{Co}_2\text{ZrSn}$ .

the valence bands can be subdivided into several regions. The lowest valence band appeared in both the majority and minority spin states between  $-11.7$  and  $-9$  eV for  $\text{Co}_2\text{TiSn}$  and between  $-11.4$  and  $-9$  eV for  $\text{Co}_2\text{ZrSn}$  is entirely due to the tin  $5s$  electrons and is separated with respect to the other hybridized bands, being basically unaffected by the Co and Ti or Zr exchange interaction. The next three energy bands in the energy region between approximately  $-7$  and  $-3$  eV are the tin  $5p$  bands. The upper dispersed bands, which are located above and below  $E_F$  from about  $-3$  to  $5$  eV, are due to the strong hybridization of Co and Ti or Zr  $d$  energy bands. The corresponding spin-projected partial densities of states are shown in figure 2.

Due to the strong Sn  $p$ - $p$  hybridization, Sn  $p$  states are split into bonding and antibonding states. The former are located between approximately  $-7$  and  $-1$  eV, while the latter are spread over a broad energy range above  $-1$  eV. The centers of Ti and Zr  $d$  states, defined as the energy at which the corresponding logarithmic derivative is equal to  $-l - 1$ , lie at  $\varepsilon_\nu = 0.76$  eV and  $\varepsilon_\nu = 1.76$  eV, respectively. The crystal field at the Ti and Zr  $4a$  site ( $O_h$  point symmetry) splits their  $d$  states into  $e_g$  and  $t_{2g}$  ones. The  $e_g$  states, which form  $\sigma$  bonds with Sn  $p$  states, are strongly hybridized with the latter and give a significant contribution to the bonding states below  $-3$  eV. The  $t_{2g}$  states form weaker Ti  $d$  - Sn  $p$  and Zr  $d$  - Sn  $p$   $\pi$  bonds but they strongly hybridize with  $d$  states of eight Co nearest neighbors.

The center of Co  $d$  states ( $\varepsilon_\nu = -1.19$  eV for Co<sub>2</sub>TiSn and  $\varepsilon_\nu = -1.08$  eV for Co<sub>2</sub>ZrSn) is found in a gap between the bonding and antibonding Sn  $p$  states. The crystal field at the Co  $4b$  site ( $T_d$  point symmetry) causes the splitting of  $d$  orbitals into a doublet  $e$  ( $d_{3z^2-1}$  and  $d_{x^2-y^2}$ ) and a triplet  $t_2$  ( $d_{xy}$ ,  $d_{yz}$ , and  $d_{xz}$ ). The hybridization between Co  $t_2$  and Ti  $t_{2g}$  states in Co<sub>2</sub>TiSn and Co  $t_2$  and Zr  $t_{2g}$  states in Co<sub>2</sub>ZrSn causes the splitting of the Ti and Zr  $t_{2g}$  states into two peaks, the bonding ones located at  $\sim 2$  eV below the Fermi level and the unoccupied antibonding peaks centered at  $\sim 1.5$  eV for Co<sub>2</sub>TiSn and at  $\sim 2.5$  eV for Co<sub>2</sub>ZrSn. The Co  $e$  orbitals are split into well separated bonding and antibonding peaks. The bonding states are rather strongly hybridized with Zr, Ti and Sn states, while the antibonding states provide a peak in the minority spin band which is located very close to the Fermi level and is quite similar between Co<sub>2</sub>TiSn and Co<sub>2</sub>ZrSn.

In addition to the crystal field splitting, the  $d$  levels of the Co, Ti and Zr atoms are split due to the exchange interaction. The exchange splitting between the spin-up and -down  $d$  electrons on the Co atom is about 0.5 eV. The corresponding splitting on the Ti and Zr atom is much smaller. Spin-orbit splitting of the  $d$  energy bands for the Co, Ti and Zr atoms is much smaller than their spin and crystal-field splittings. In the vicinity of the Fermi energy the minority spin bands of both alloys show a gap (at  $E = -0.18$  eV for Co<sub>2</sub>TiSn and at  $E = -0.14$  eV for Co<sub>2</sub>ZrSn). However, the Fermi level crosses both the majority and minority spin energy bands, so neither Co<sub>2</sub>TiSn nor Co<sub>2</sub>ZrSn are half-metallic ferromagnets.

### 3.2. XMCD spectra

At the core level edge XMCD is not only element-specific but also orbital specific. For  $3d$  transition metals, the electronic states can be probed by the  $K$ ,  $L_{2,3}$  and  $M_{2,3}$  x-ray absorption and emission spectra whereas in  $4d$  transition metals one can use the  $K$ ,  $L_{2,3}$ ,  $M_{2,3}$  and  $M_{4,5}$  spectra.

The experimentally measured dichroic lines have different signs at the  $L_3$  and  $L_2$  edges [18]. In order to compare relative amplitudes of the  $L_3$  and  $L_2$  XMCD spectra we first normalize the corresponding isotropic x-ray absorption spectra (XAS) to the experimental ones taking into account the background scattering intensity as described in section 2. Figure 3 shows the calculated isotropic x-ray absorption and XMCD spectra of Co at the  $L_{2,3}$  edges for both alloys in the LSDA approach together with the experimental data [18]. The contribution from the background scattering is shown by dotted line in the XAS panels of figure 3.

Because of the dipole selection rules, apart from the  $4s_{1/2}$  states (which have a small contribution to the XAS due to relatively small  $2p \rightarrow 4s$  matrix elements) only  $3d_{3/2}$  states occur as final states for  $L_2$  XAS for unpolarized radiation, whereas for the  $L_3$  XAS  $3d_{5/2}$  states also contribute [29]. Although the  $2p_{3/2} \rightarrow 3d_{3/2}$  radial matrix elements are only slightly smaller than for the  $2p_{3/2} \rightarrow 3d_{5/2}$  transitions the angular matrix elements strongly suppress the  $2p_{3/2} \rightarrow 3d_{3/2}$  contribution [29]. Therefore in neglecting the energy dependence of the radial matrix elements, the  $L_2$  and the  $L_3$  spectra can be viewed as a direct mapping of the DOS curve for  $3d_{3/2}$  and  $3d_{5/2}$  character, respectively. The XMCD spectra at the  $L_{2,3}$  edges are mostly determined

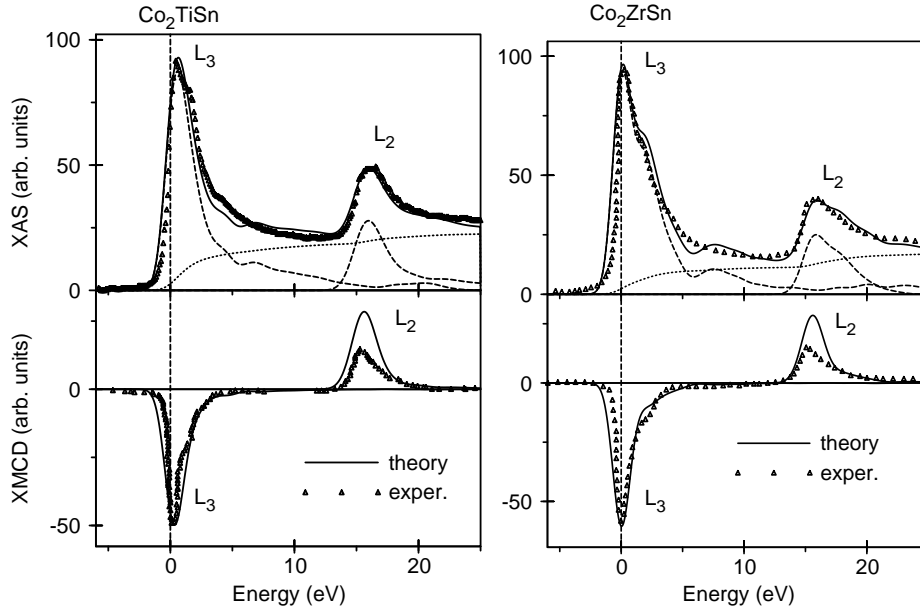


**Figure 3.** Theoretically calculated (full line) and experimental (triangles) isotropic absorption and XMCD spectra of  $\text{Co}_2\text{TiSn}$  and  $\text{Co}_2\text{ZrSn}$  at the Co  $L_{2,3}$  edges. Experimental spectra [18] were measured at 50 K. The XAS panel also shows the background spectra (dotted line) due to the transitions from inner  $2p_{1/2,3/2}$  levels to the continuum of unoccupied levels [27].

by the strength of the SO coupling of the initial  $2p$  core states and spin-polarization of the final empty  $3d_{3/2,5/2}$  states while the exchange splitting of the  $2p$  core states as well as the SO coupling of the  $3d$  valence states are of minor importance for the XMCD at the  $L_{2,3}$  edge of  $3d$  transition metals [29]. The theoretically calculated Co  $L_{2,3}$  XMCD spectra are in good agreement with the experiment, although the calculated magnetic circular dichroism is somewhat too high at the  $L_2$  edge. The main reason for this discrepancy is the core-hole effect. When the  $2p$  core electron is photo-excited to the unoccupied  $d$  states, the distribution of the charge changes to account for the hole created. This effect is not taken into account by the electronic structure calculations and leads to the observed discrepancy [30].

### 3.3. Magnetic properties

In magnets, the atomic spin  $M_s$  and orbital  $M_l$  magnetic moments are basic quantities and their separate determination is therefore important. Methods of their experimental determination include traditional gyromagnetic ratio measurements [31], magnetic form factor measurements using neutron scattering [32], and magnetic x-ray scattering [33]. In addition to these, the recently developed x-ray magnetic circular dichroism combined with several sum rules [34,35] has attracted much attention as a method of site- and symmetry-selective determination of  $M_s$  and  $M_l$ . Table 1 presents the comparison between calculated and experimental magnetic mo-



**Table 1.** The experimental and calculated spin  $M_s$  and orbital  $M_l$  magnetic moments (in  $\mu_B$ ) of  $\text{Co}_2\text{TiSn}$  and  $\text{Co}_2\text{ZrSn}$ .

	atom	$M_s$	$M_l$		atom	$M_s$	$M_l$
$\text{Co}_2\text{TiSn}$	Co	0.741	0.037	$\text{Co}_2\text{ZrSn}$	Co	0.864	0.052
	Ti	-0.101	0.010		Zr	-0.107	0.009
	Sn	0.021	0.001		Sn	0.029	0.001
sum rules	Co	0.525	0.024	sum rules	Co	0.604	0.034
sum rules <sup>a</sup>	Co	0.692	0.036	sum rules <sup>a</sup>	Co	0.795	0.050
sum rules <sup>b</sup>	Co	0.707	0.037	sum rules <sup>b</sup>	Co	0.811	0.051
experiment <sup>c</sup>	Co	0.87	0.09	experiment <sup>c</sup>	Co	0.70	0.12

<sup>a</sup>sum rules applied for the XMCD spectra calculated with ignoring the energy dependence of the radial matrix elements.

<sup>b</sup>sum rules applied for the XMCD spectra calculated with ignoring the energy dependence of the radial matrix elements and ignoring  $p \rightarrow s$  transitions.

<sup>c</sup>Reference [18].

ments in  $\text{Co}_2\text{TiSn}$  and  $\text{Co}_2\text{ZrSn}$ . The spin magnetic moment at the tin site is very small. The spin moment at the Ti and Zr sites is also small and has an opposite direction to the spin moment at the Co sites. In  $\text{Co}_2\text{ZrSn}$  the spin moment on the Co atom is larger than in  $\text{Co}_2\text{TiSn}$ ; this can be ascribed to the larger lattice constant of the Co sublattice in  $\text{Co}_2\text{ZrSn}$ , which results in a smaller Co  $3d$ 's direct hybridization and a consequently larger exchange interaction. It is generally believed in transition-metal compounds that the orbital contribution becomes larger when the  $3d$  states are more localized [36]. Therefore, our results for the orbital moment also suggest that the Co  $3d$  states are more localized in  $\text{Co}_2\text{ZrSn}$  than in  $\text{Co}_2\text{TiSn}$ . The calculated total magnetic moment for  $\text{Co}_2\text{TiSn}$  is  $1.402 \mu_B/\text{f.u.}$  and for  $\text{Co}_2\text{ZrSn}$  it is  $1.650 \mu_B/\text{f.u.}$  while the experimental values [18] for these alloys are  $1.92 \mu_B/\text{f.u.}$  and  $1.64 \mu_B/\text{f.u.}$ , respectively.

It is interesting to compare the spin and orbital moments obtained from the theoretically calculated XAS and XMCD spectra through sum rules [Equations (4),(5)] with directly calculated LSDA values. In this case we at least avoid all the experimental problems. The number of the Co  $3d$  electrons is calculated by integrating the occupied  $d$  partial density of states inside the corresponding atomic sphere which gives the values  $n_{\text{Co}}=7.871$  for  $\text{Co}_2\text{TiSn}$  and  $n_{\text{Co}}=7.892$  for  $\text{Co}_2\text{ZrSn}$ . Sum rules reproduce the spin magnetic moments within 30% and the orbital moments within 35% for both  $\text{Co}_2\text{TiSn}$  and  $\text{Co}_2\text{ZrSn}$  (table 1). XMCD sum rules for  $L_{2,3}$  are derived within an ionic model using a series of approximations, particularly disregarding the energy dependence of the radial matrix elements and  $p \rightarrow s$  transitions [37]. To investigate the effect of these two factors we applied the sum rules to the XMCD spectra calculated neglecting the energy dependence of the radial matrix elements and the  $p \rightarrow s$  transitions. As can be seen from table 1 using the energy independent radial matrix elements reduces the disagreement in spin magnetic moments to 7% and 8% and in the orbital moment to 3% and 4% for  $\text{Co}_2\text{TiSn}$  and  $\text{Co}_2\text{ZrSn}$ , re-

spectively. An additional omission of the  $p \rightarrow s$  transitions reduces the discrepancy between LSDA and the sum rule results up to 5% and 6% for the spin moments and  $\sim 0\%$  and 3% for the orbital moments for  $\text{Co}_2\text{TiSn}$  and  $\text{Co}_2\text{ZrSn}$ , respectively. These results show that the energy dependence of the matrix elements and the presence of  $s \rightarrow p$  transitions strongly affect the values of both the spin and the orbital magnetic moments derived using the sum rules.

The values of the orbital magnetic moment derived from the experimental XMCD spectra ( $M_l^{\text{exp}}=0.09 \mu_B$  for  $\text{Co}_2\text{TiSn}$  and  $M_l^{\text{exp}}=0.12 \mu_B$  for  $\text{Co}_2\text{ZrSn}$  [18]) are considerably higher in comparison with our band structure calculations. It is a well-known fact, however, that LSDA calculations be inaccurate in describing orbital magnetism [29,37]. In the LSDA, the Kohn-Sham equation is described by a local potential which depends on the electron spin density. The orbital current, which is responsible for  $M_l$ , is, however, not included in the equations. This means, that although  $M_s$  is self-consistently determined in the LSDA, there is no framework to determine simultaneously  $M_l$  self-consistently. To calculate  $M_l$  beyond the LSDA scheme we used the rotationally invariant LSDA+ $U$  method [38]. We used  $U_{\text{eff}} = 0$  ( $U = J = 1.0 \text{ eV}$ ). In this case the effect of the LSDA+ $U$  comes from non-spherical terms and the approach is similar to the orbital polarization corrections [29]. The LSDA+ $U$  calculations produced the orbital magnetic moments for  $\text{Co}_2\text{TiSn}$  and  $\text{Co}_2\text{ZrSn}$  equal to  $0.057 \mu_B$  and  $0.074 \mu_B$  per Co atom, respectively. These values are in better agreement with the experimental data but still smaller than the experimental estimations.

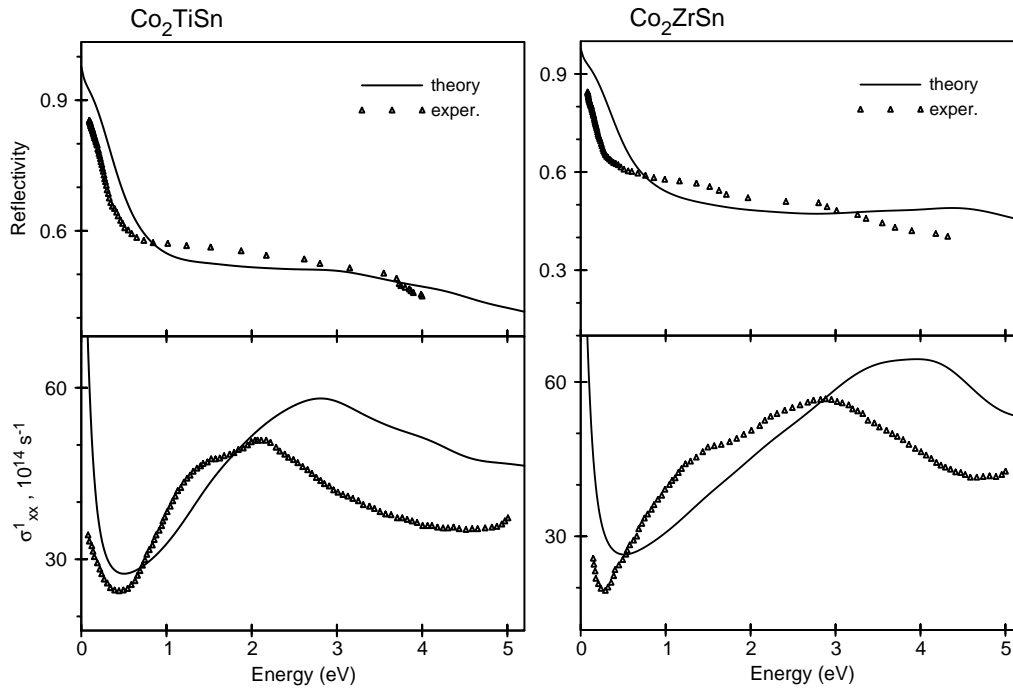


**Figure 4.** Theoretically calculated (full line) and experimentally measured [19] (triangles) reflectivity  $R(\omega)$  and diagonal  $\sigma_{xx}^1$  absorptive part of optical conductivity tensor for  $\text{Co}_2\text{TiSn}$  and  $\text{Co}_2\text{ZrSn}$ .

### 3.4. Optical properties

The optical properties of materials originate from interband transitions from occupied to unoccupied bands, involving not only the occupied and unoccupied parts of the electronic structure but also the character of the bands.

Figure 4 shows the results of our calculations of the reflectivity  $R(\omega)$  and the diagonal  $\sigma_{xx}^1(\omega)$  absorptive part of optical conductivity tensor in comparison with the experimental energy dependences of these constants [19]. The theoretical reflectivity spectra are in good agreement with the experimental data. Both theory and experiment give a rather sharp slope of reflectivity at low energies and then a slow decreasing behaviour. Theory overestimates the slope region within about 0.5 eV for both alloys and the reflectivity values in that region.

The positions of the  $\sigma_{xx}^1$  maxima for both alloys are about 1 eV overestimated by theory, and their theoretical values are larger than the experimental ones. The theoretical spectra of  $\sigma_{xx}^1$  at low energies have a pronounced Drude-like behaviour, while the experimental ones exhibit a decrease of the Drude contribution to  $\sigma_{xx}^1$ . The main reason of this discrepancy is an arrangement disorder of the Sn, Ti and Zr atoms in the experimentally investigated alloys [19], which results in a sharp increase of the conduction electron scattering. The authors of [19] also believe that the decrease of the Drude contribution to  $\sigma_{xx}^1$  observed in the experimentally considered alloys is partly caused by their half-metallic nature. However, as we have pointed out, our fully relativistic calculations predict that  $\text{Co}_2\text{TiSn}$  and  $\text{Co}_2\text{ZrSn}$  are not half-metallic ferromagnets.

## 4. Summary

We have studied by means of a fully relativistic spin-polarized Dirac linear muffin-tin orbital method the electronic and magnetic structures as well as optical properties and x-ray magnetic circular dichroism spectra of  $\text{Co}_2\text{TiSn}$  and  $\text{Co}_2\text{ZrSn}$ . The most characteristic features of the Co  $d$  states are an antibonding peak in the minority spin band which is located very close to the Fermi level and is quite similar between  $\text{Co}_2\text{TiSn}$  and  $\text{Co}_2\text{ZrSn}$ , and an energy gap at  $E = -0.18$  eV for  $\text{Co}_2\text{TiSn}$  and at  $E = -0.14$  eV for  $\text{Co}_2\text{ZrSn}$  in the minority spin band. The spin moment in both alloys has a significant value only for the Co atoms, and for  $\text{Co}_2\text{ZrSn}$  it is greater than for  $\text{Co}_2\text{TiSn}$ ; its values for the other atoms are close to zero. The total magnetic moment of  $\text{Co}_2\text{ZrSn}$  is very close to its experimental value and in contrast to the experiment is larger than that of  $\text{Co}_2\text{TiSn}$ , while for the latter it is 27% smaller than the experimental result. The calculated reflectivity spectra are in good agreement with the experimental data. The theoretical spectra of  $\sigma_{xx}^1$  at low energies in contrast to the experiment have a pronounced Drude-like behaviour. The x-ray absorption and XMCD spectra at the Co  $L_{2,3}$  edges are reproduced quite well by our LSDA band structure calculations, although the calculated magnetic circular dichroism is somewhat too high at the  $L_2$  edge due to the core-hole effect.

## Acknowledgements

This work was supported by the CRDF program, project No. 14589.

## References

1. Webster P.J., Ziebeck K.R.A., Alloys and Compounds of d-Elements with Main Group Elements. Part 2, edited by Wijn H.R.J., vol. 19/C of *Landolt-Börnstein, New Series, Group III*, 75–184, Springer-Verlag, Berlin, 1988.
2. Pierre J., Skolozdra R.V., Tobola J., Kaprzyk S., Hordequin C., Kouacou M.A., Karla I., Currat R., Lelièvre-Berna E., *J. Alloys Comp.*, 1997, **262–263**, 101.
3. Tobola J., Pierre J., *J. Alloys Comp.*, 2000, **296**, 243.
4. Prinz G.A., *Science*, 1998, **282**, 1660.
5. Ohno Y., Young D.K., Beschoten B., Matsukura F., Ohno H., Awschalom D.D., *Nature*, 1999, **402**, 790.
6. Dietl T., Ohno H., Matsukura F., Cibert J., Ferrand D., *Science*, 2000, **287**, 1019.
7. Park J.H., Vescovo E., Kim H.J., Kwon C., Ramesh R., Venkatesan T., *Nature*, 1998, **392**, 794.
8. Deb A., Itou M., Sakurai Y., Hiraoka N., Sakai N., *Phys. Rev. B*, 2001, **63**, 064409.
9. de Groot R.A., Mueller F.M., van Engen P., Buschow K.H.J., *Phys. Rev. Lett.*, 1983, **50**, 2024.
10. Pickett W., *Phys. World*, 1998, **11**, 22.
11. Galanakis I., Ostanin S., Alouani M., Dreyssé H., Wills J.M., *Phys. Rev. B*, 2000, **61**, 4093.
12. Ziebeck K.R.A., Webster P.J., *J. Phys. Chem. Solids*, 1974, **35**, 1.
13. Gorlich E.A., Kmiec R., Latka K., Matlak T., Ruebenbauer K., Szytula A., Tomala K., *Phys. Status Solidi A*, 1975, **30**, 765.
14. Ishida S., Akazawa S., Kubo Y., Ishida J., *J. Phys. F: Met. Phys.*, 1982, **12**, 1111.
15. van Engen P.G., Buschow K.H.J., Erman M., *J. Magn. Magn. Mater.*, 1983, **30**, 374.
16. Pierre J., Skolozdra R.V., Stadnyk Y.V., *J. Magn. Magn. Mater.*, 1993, **128**, 93.
17. Ślebarski A., Jezierski A., Lütkehoff S., Neumann M., *Phys. Rev. B*, 1998, **57**, 6408.
18. Yamasaki A., Imada S., Arai R., Utsunomiya H., Suga S., Muro T., Saitoh Y., Kanomata T., Ishida S., *Phys. Rev. B*, 2002, **65**, 104410.
19. Shreder E.I., Kirillova M.M., Dyakina V.P., *Phys. Met. Metallogr.*, 2000, **90**, No. 4, 48 (in Russian).
20. Andersen O.K., *Phys. Rev. B*, 1975, **12**, 3060.
21. Nemoshkalenko V.V., Krasovskii A.E., Antonov V.N., Antonov V.N., Fleck U., Wonn H., Ziesche P., *Phys. Status Solidi B*, 1983, **120**, 283.
22. von Barth U., Hedin L., *J. Phys. C*, 1972, **5**, 1629.
23. Blöchl P.E., Jepsen O., Andersen O.K., *Phys. Rev. B*, 1994, **49**, 16.
24. Alouani M., Wills J.M., *Phys. Rev. B*, 1996, **54**, 2480.
25. Ahuja R., Auluck S., Wills J.M., Alouani M., Johansson B., Eriksson O., *Phys. Rev. B*, 1997, **55**, 4999.
26. Kleiner W.H., *Phys. Rev.*, 1966, **142**, 318.
27. Richtmyer F.K., Barnes S.W., Ramberg E., *Phys. Rev.*, 1934, **46**, 843.
28. Fuggle J.C., Inglesfield J.E., *Unoccupied Electronic States. Topics in Applied Physics*, vol. 69. Springer, New York, 1992.

29. Antonov V., Harmon B., Yaresko A., Electronic structure and magneto-optical properties of solids. Kluwer Academic Publishers, Dordrecht, Boston, London, 2004.
30. Schwitalla J., Ebert H., Phys. Rev. Lett., 1998, **80**, 4586.
31. Scott G.G., J. Phys. Soc. Jpn., 1962, **17**, 372.
32. Marshall W., Lovsey S.W., Theory of Thermal Neutron Scattering. Oxford University Press, Oxford, 1971.
33. Blume M., J. Appl. Phys., 1985, **57**, 3615.
34. Thole B.T., Carra P., Sette F., van der Laan G., Phys. Rev. Lett., 1992, **68**, 1943.
35. Carra P., Thole B.T., Altarelli M., Wang X., Phys. Rev. Lett., 1993, **70**, 694.
36. Okutani M., Jo T., J. Phys. Soc. Jpn., 2000, **69**, 598.
37. Ebert H., Rep. Prog. Phys., 1996, **59**, 1665.
38. Yaresko A.N., Antonov V. N., Fulde P., Phys. Rev. B, 2003, **67**, 155103.

### **Електронна структура та властивості збудженого стану $\text{Co}_2\text{TiSn}$ та $\text{Co}_2\text{ZrSn}$ , отримані з *ab initio* розрахунків**

Л.В.Бекенов<sup>1</sup>, В.М.Антонов<sup>1</sup>, А.П.Шпак<sup>1</sup>,  
О.М.Яресько<sup>2</sup>

<sup>1</sup> Інститут металофізики ім. Г.В.Курдюмова НАН України,  
бульв. Вернадського 36, 03142 Київ

<sup>2</sup> Інститут Макса Планка Комплексних систем,  
D-01187 Дрезден, Німеччина

Отримано 24 червня 2005 р.

Використовуючи повністю релятивістський діраківський ЛМТО метод зонних розрахунків було теоретично досліджено електронну структуру, магнітні властивості та властивості збудженого стану, такі як оптичні спектри та спектри рентгенівського магнітного циркулярного дихроїзму, сплавів Гейслера  $\text{Co}_2\text{TiSn}$  та  $\text{Co}_2\text{ZrSn}$ . з'ясовано походження  $L_{2,3}$ -спектрів рентгенівського циркулярного магнітного дихроїзму на атомах кобальту. Проаналізовано та обговорено щільності валентних станів, величини орбітального та спінового магнітних моментів та оптичні спектри. Результати розрахунків порівняно з експериментальними даними.

**Ключові слова:** електронна структура, сплави Гейслера, рентгенівський магнітний циркулярний дихроїзм, оптичні властивості

**PACS:** 71.28.+d, 71.25.Pi, 75.30.Mb

